

Deep Learning-Based Automatic Design System for IPMSM with Variable Magnet Properties

Yuki Shimizu
College of Science and Engineering/ N/A
Ritsumeikan University/ MotorAI Inc.
Kusatsu, Japan
yshimizu@fc.ritsumei.ac.jp

Kan Akatsu
Faculty of Engineering
Yokohama National University
Yokohama, Japan
akatsu-kan-py@ynu.ac.jp

Abstract—Interior permanent magnet synchronous motors are highly valued in electric vehicles for their performance, efficiency, and reliability. Optimizing their design often requires time-consuming finite element analysis. Deep learning can accelerate the design of interior permanent magnet synchronous motor, providing a faster alternative to finite element analysis. This study proposes a deep learning model capable of handling various inputs and outputs, including permanent magnet properties and temperatures. This system allows efficient optimization across different rotor designs and conditions, with the benefit of multiple iterations after training.

Keywords— IPMSM, deep learning, generative adversarial network, shape optimization, and magnet material

I. INTRODUCTION

Known for their high power, efficiency, and reliability, interior permanent magnet synchronous motors (IPMSMs) have become increasingly popular as traction motors in electric vehicles. The process of optimizing the geometry design of IPMSMs typically involves extensive finite element analysis (FEA), resulting in significant computational time. To address this challenge, there is growing interest in the use of machine learning (ML)-based surrogate models, which provide a faster design optimization alternative without the need for FEA.

Many studies [1]–[3] have aimed to speed up the optimal design of advanced IPMSMs using ML. Although ML requires training time, it's much faster than FEA, requiring, for example, less than 1/1000 of the time after the model is

trained [4]. There are two types of studies. One uses motor geometrical parameters and current conditions as input for accurate predictions suitable after initial design. The other analyzes rotor geometry material data as tensors with deep learning (DL) using tools such as convolutional neural networks (CNN) and vision transformers (ViTs), allowing for different topologies but increasing training data, model size, and time.

The studies have limitations in terms of input and output characteristics. Therefore, this study proposes a DL model that accommodates various inputs and outputs, especially including different permanent magnet (PM) characteristics and temperatures, and develops an automatic IPMSM design system as shown in Fig. 1. In this system, the rotor geometry of the IPMSM is designed using a generative adversarial network (GAN), which enables rapid prediction of speed, torque, and iron loss using two prediction models. This method allows efficiency optimization over many rotor topologies for any speed and torque configuration. Another advantage is the ability to perform multiple iterative optimizations after training. The more data and the larger the model, the more analysis and training time it takes, but the more users can use it many times for a wider variety of applications, resulting in a time advantage.

II. AUTOMATIC DESIGN SYSTEM

A. Target Motor

The method proposed in this study is not limited to a specific application. To validate the generality of the proposed method, the following discussion focuses on automotive IPMSMs, which require a wide operating range.

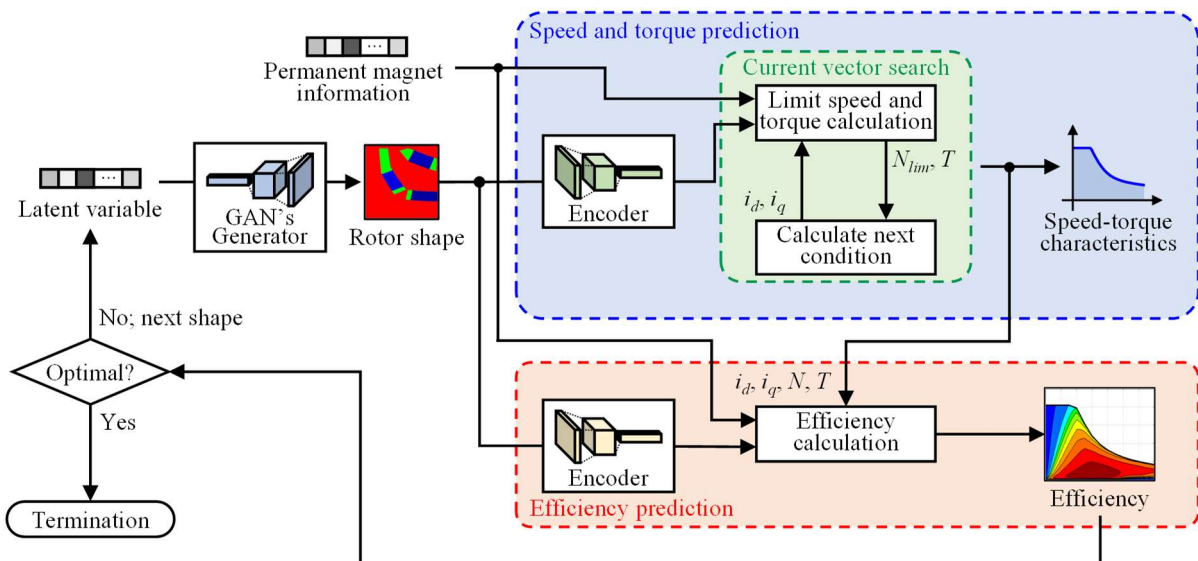


Fig. 1. Overall configuration of automatic design system with variable permanent magnet properties. The blue part represents the prediction for the speed and torque characteristics, and the red part represents the prediction for the iron loss characteristic. i_d and i_q are the d - and q -axis currents, respectively, N is the motor speed, N_{lim} is the limit motor speed, and T is the torque.

Fig. 2 shows a cross-sectional view of the IPMSM subject of this study (for one pole), and Table I shows the specifications common to all IPMSMs used. In the automatic design system of this study, the stator shape, body size, and core material shown in Fig. 2 are fixed, while the rotor shape, PM material, and current, speed, and temperature conditions are variable.

B. Training Dataset

A training dataset for deep learning was generated using FEA based on the motor geometry in Fig. 2. Fig. 3 shows the rotor topologies used in the dataset, and Table II shows the range of FEA conditions. For the shapes, 10,000 shapes for each topology were generated by combining randomly generated dimensional parameters and CAD software based on the four types of rotor topologies shown in Fig. 3. For each of these 10,000 shapes, 10 different PM materials listed in Table II were combined to create 100,000 different rotors for each topology. Six types of sintered Nd magnets from Proterial, Ltd. and four types of SmCo magnets from Shin-Etsu Chemical Co., Ltd. were used to cover a wide range of magnetic and temperature characteristics.

FEA conditions were then determined for the generated rotors. For current amplitude, current phase, motor speed, and PM temperature, 300,000 FEA conditions were generated using the upper and lower bounds in Table II and the Latin hypercube method. A total of 1.2 million FEA cases were performed for four different rotor topologies by using each of the 100,000 rotors for each topology three times in duplicate. The motor characteristics calculated were d - and q -axis magnetic flux and core iron loss (hysteresis loss and eddy current loss). The magnetic flux characteristics were calculated from vector potentials from electromagnetic field analysis, the iron loss was calculated from FFT results of magnetic flux density, and a dual-frequency separation method [5] was used to separate hysteresis loss and eddy current loss. To reduce computation time, sinusoidal current inputs were used, and the effect of PWM inverters was not considered. JMAG-Designer 22.0 was used for the analysis, and a total of 1,199,370 data sets were generated, excluding cases where the analysis failed. The analysis was performed on a PC with an AMD EPYC 7763 64-core \times 2 processor and the total analysis time was 322.94 hours. Of course, the more data to analyze, the larger the analysis calculation. However, the generality of the model improves, allowing many users to use it many times for a wide range of applications, resulting in a time advantage.

C. Motor Design by Deep Generative Model

This study focuses on different rotor topologies and tries to handle them in a harmonious way by representing rotor geometries as images. Fig. 4 shows a schematic of the material representation approach implemented in the system. The rotor pole coordinates are specified as electrical steel sheets, PMs, or air. The image represents the rotor configuration by assigning one-hot vectors to the 256 \times 256 RGB pixels for each of the three materials, as shown in the right part of Fig. 4. A GAN generates the rotor image from a 256-dimensional latent variable space as follows.

$$\mathbf{x}_{rotor} = \mathcal{G}(\mathbf{z}), \quad (1)$$

where \mathcal{G} is the generator of the GAN, \mathbf{x}_{rotor} is the generated rotor image, \mathbf{z} is the latent variable. See [6] for more details.

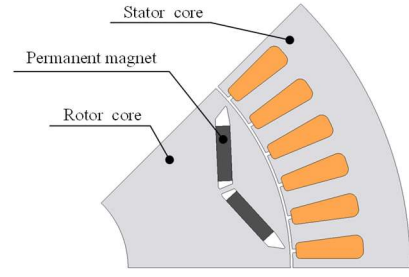


Fig. 2. Cross section of target motor (single pole).

TABLE I. COMMON SPECIFICATION OF TARGET MOTOR

Item	Value
Number of pole/slot	8/48
Stator outer diameter	204 mm
Rotor outer diameter	69.3 mm
Air gap length	0.7 mm
Shaft diameter	50 mm
Stack length	100 mm
Winding resistance	0.05 Ω
Number of turns	7
Core material	35JNE300

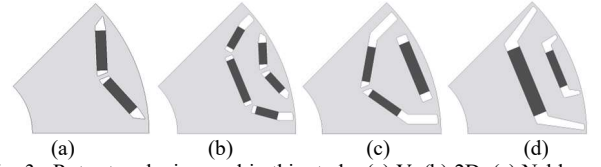


Fig. 3. Rotor topologies used in this study. (a) V, (b) 2D, (c) Nabla, and (d) 2U.

TABLE II. CONDITION FOR FEA OF TRAINING DATASET

Item	Range
Current amplitude	0 – 800 A
Phase of current	0 – 90°
Motor speed	0 – 30,000 r/min
Permanent magnet temperature	0 – 200 °C
Permanent magnet material	NMX-K30ER, NMX-34EH, NMX-39EH, NMX-43SH, NMX-S49CH, NMX-S52, R26HE, R30, R32HS, R33H

D. Characteristic Prediction by Vision Transformer

By predicting the characteristics from the generated images, an automatic design system can be constructed without FEA. This study uses geometry, driving conditions, and PM property information as input data, and considers models for predicting motor parameters and iron loss as follows.

$$\Psi_d, \Psi_q = \mathcal{F}_{flux}(\mathbf{x}_{rotor}, \mathbf{x}_{PM}, \mathbf{c}_{flux}), \quad (2)$$

$$W_h, W_e = \mathcal{F}_{iron}(\mathbf{x}_{rotor}, \mathbf{x}_{PM}, \mathbf{c}_{iron}), \quad (3)$$

where \mathcal{F}_{flux} and \mathcal{F}_{iron} are the prediction models for the magnetic flux linkages and the iron losses, respectively, Ψ_d and Ψ_q are the d - and q -axis flux linkages, respectively, and W_h and W_e are hysteresis loss and eddy current loss, respectively. $\mathbf{x}_{PM} \in \mathbb{R}^7$ is the vector of properties and temperature of the PM, and $\mathbf{c}_{flux} = (i_d, i_q)^T \in \mathbb{R}^2$ and $\mathbf{c}_{iron} = (i_d, i_q, N)^T \in \mathbb{R}^3$ are the driving condition, where i_d and i_q are the d - and q -axis currents, respectively, and N is the motor speed.

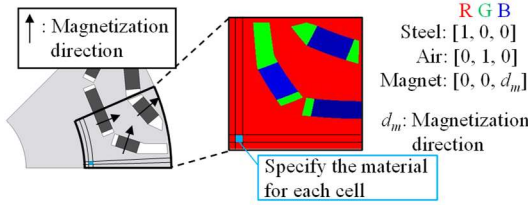


Fig. 4. Schematic of material representation of rotor shape.

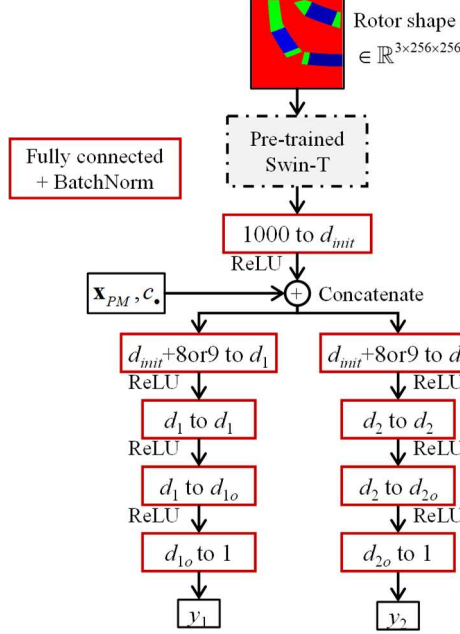


Fig. 5. Common architecture of prediction models for flux linkages and iron losses.

These models allow prediction of torque and efficiency characteristics under various current vector control conditions as follows.

$$T = P_n (\Psi_d i_q - \Psi_q i_d) \text{ (Nm)}, \quad (4)$$

$$N_{lim} = \frac{V_{om}}{\sqrt{\Psi_d^2 + \Psi_q^2}} \times \frac{60}{2\pi} \text{ (r/min)}, \quad (5)$$

$$\eta = \frac{\omega_m T}{\omega_m T + R_a I_a^2 + W_i} \times 100 = \frac{\omega_m T}{\omega_m T + R_a I_a^2 + W_h + W_e} \times 100 \text{ (%)}, \quad (6)$$

where P_n is the number of pole pairs, R_a is the winding resistance, V_{om} is the maximum induced voltage, ω_m is the mechanical angular frequency, and W_i is the iron loss. The limit speed is calculated. The current conditions driving each speed and torque point are determined according to the maximum power control algorithm [7] under current and voltage limits. The iron loss is calculated by inputting the searched current and speed conditions into the iron loss prediction model, and the efficiency at each speed and torque point is calculated according to (6).

Fig. 5 shows the common architecture of the prediction models for flux linkages and iron losses, and Table III lists their hyperparameters. As input, a trained model that encodes the rotor image generated by the GAN is used to extract the semantic rotor geometry data from the image. In this study, the pre-trained Swin Transformer (Swin-T) [8] is used as the encoding model. The resulting shape encoding information is combined with the PM characteristics and the FEA driving conditions in a multi-task training. The PM characteristics and

TABLE III. HYPERPARAMETERS FOR PREDICTION MODELS

Items	Value (flux)	Value (iron)
d_{init}	4	8
d_1	16	16
d_2	8	8
d_{1o}	50	50
d_{2o}	50	50
Learning rate	0.001	0.006325

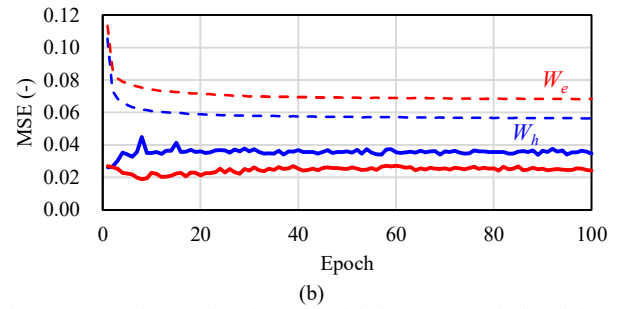
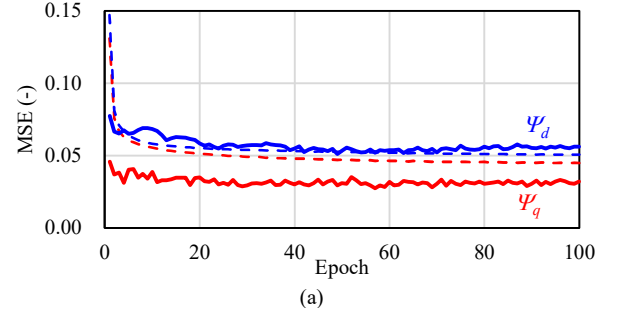


Fig. 6. Training losses of prediction models for (a) magnetic flux linkages and (b) iron losses. The dashed line is the loss to training data and the bold line is the loss to validation data.

the FEA driving conditions are standardized according to the following equations.

$$\bar{X} = \frac{X - \mu_X}{\sigma_X} \quad (X \in \{i_d, i_q, N\}), \quad (7)$$

where μ_X and σ_X are the mean and standard deviation of the training data, respectively. The multilayer perceptron (MLP) consists of fully connected layers and batch normalization, with a rectified linear unit (ReLU) serving as the activation.

$$Z^{(l+1)} = \phi \left(BN_{\gamma^{(l)}, \beta^{(l)}} \left(W^{(l)} Z^{(l)} + B^{(l)} \right) \right), \quad (8)$$

$$BN_{\gamma^{(l)}, \beta^{(l)}} \left(X^{(l)} \right) = \gamma^{(l)} \frac{X^{(l)} - \mathbb{E}[X^{(l)}]}{\sqrt{\text{Var}[X^{(l)}] + \varepsilon}} + \beta^{(l)}, \quad (9)$$

$$\phi(X^{(l)}) = \text{ReLU}(X^{(l)}) = \max(X^{(l)}, 0), \quad (10)$$

where $Z^{(l)}$ is the input to the l -layer, $W^{(l)}$ and $B^{(l)}$ are the weights and biases of the l -layer to be trained. In the batch normalization, the mean and standard deviation are computed per dimension over the mini-batches, $\gamma^{(l)}$ and $\beta^{(l)}$ are the learnable parameter vectors, and $\varepsilon = 0.00001$ is a constant added to the mini-batch variance for numerical stability. The hyperparameters listed in Table III are manually optimized by comparative study [9].

80% of the dataset was used for training, while the remaining 20% was used for validation. The mean squared

error (MSE) determined the loss function for multitask learning, as shown in the following equation.

$$\mathcal{L} = \mathcal{L}_1 + \mathcal{L}_2 = \frac{1}{n} \left(\sum_{i=1}^n (y_1^{(i)} - \hat{y}_1^{(i)})^2 + \sum_{i=1}^n (y_2^{(i)} - \hat{y}_2^{(i)})^2 \right), \quad (11)$$

where $y^{(i)}$ and $\hat{y}^{(i)}$ are the predicted characteristics and training data, respectively.

The number of training epochs was set to 100. The optimizer was Adam and the batch size was set to 128. PyTorch was used to implement the neural network model. Fig. 6 shows the losses during training. The flux prediction progresses adequately during training, but the iron loss prediction tends to be slightly underfitting.

III. NUMERICAL EXPERIMENT

The combination of the models described in Sec. II results in the automatic design system for the IPMSM rotor core as shown in Fig. 2. With this design system, the characteristics of a large number of solution shapes can be computed at high speed in the 256-dimensional latent variable space of the deep generative model. The optimization algorithm used in Sec. III was NSGA-II [10], and the pymoo library [11] was used for implementation. The population size was 100, and the number of offspring was 10. Latin hypercube sampling was used to sample the initial population, the tournament method was used for selection, simulated binary crossover was used for crossover, and polynomial mutation was used for mutation. The termination condition was set to 50 generations.

A. Efficiency Optimization

The constructed automatic design system is used to perform efficiency maximization design. The search space is a 256-dimensional latent variable space as shown in Fig. 1, and the torque-constrained efficiency maximization problem is defined as follows

$$\begin{aligned} \min_z & \quad (-\eta_1^{pred}, -\eta_2^{pred})^T, \\ \text{s.t.} & \quad g_i : T_i^{pred} \geq \alpha T_i^{req} \quad (i = 3, 4), \end{aligned} \quad (12)$$

where η_1^{pred} and η_2^{pred} are the predicted efficiencies at operating points P_1 (3,500 r/min, 50 Nm) and P_2 (11,000 r/min, 50 Nm). The constraint conditions g_i are the torque constraints for two required operating points P_3 (3,500 r/min, 197 Nm) and P_4 (11,000 r/min, 40 Nm), with a coefficient ($\alpha=1.05$) to account for the prediction error. Current conditions for torque and efficiency calculations were determined by maximum torque per ampere (MTPA) control and flux weakening (FW) control algorithm [7].

The optimization was performed with a phase current limit of 300 Arms and a DC link voltage of 650 V. Fig. 7 shows the optimization results for NMX-39CH and a PM temperature of 60 °C. Fig. 8 shows the difference in the Pareto front for PM materials at PM temperatures of 60 and 180 °C. The optimization calculations were completed in 595.5 ± 46.7 seconds per run.

It was found that the shape on the Pareto front under the NMX-39CH at 60 °C is mostly Nabla. When examining the difference by PM material, the loss at P_1 was smaller and the loss at P_2 was larger for Nd sintered magnets than for SmCo magnets at 60 °C. The loss at P_2 was greater for Nd sintered magnets than for SmCo magnets at 60 °C. The loss at P_2 was larger for Nd sintered magnets at 60 °C. This is because using

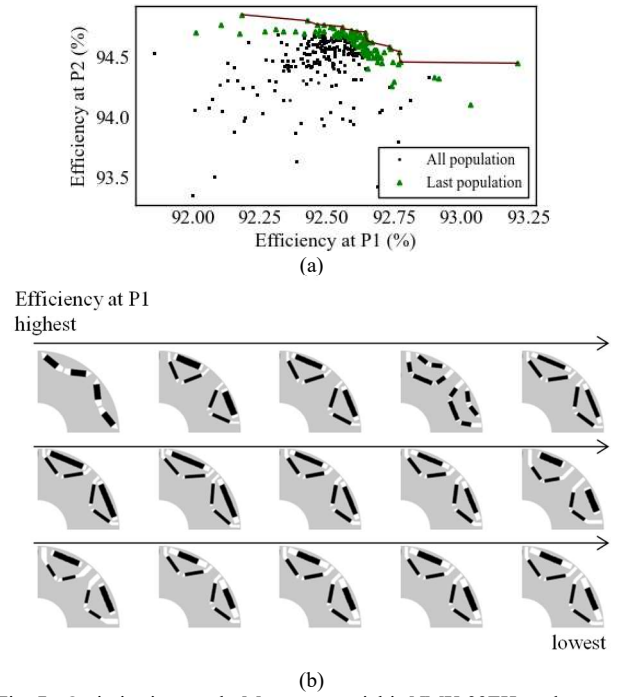


Fig. 7. Optimization result. Magnet material is NMX-39EH, and magnet temperature is 60 °C. (a) Efficiency characteristics, where red line represents Pareto front. (b) Rotor shapes of Pareto front, which are zigzagged by efficiencies at P_1 from upper left to lower right.

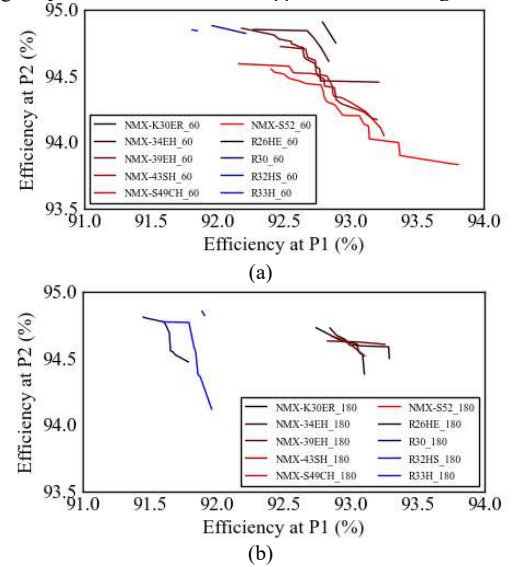


Fig. 8. Pareto fronts of optimization results under different magnet material for (a) 60 °C and (b) 180 °C. Only solutions that satisfy the torque constraint are displayed.

a PM with a large residual flux density at low speeds makes it easier to obtain torque and reduce copper loss, while at high speeds the amount of current required for weak flux control and the fundamental wave of iron loss increase. Therefore, even among Nd sintered magnets, motors using higher grade PMs had lower losses at low speeds and higher losses at high speeds. The Pareto front range of the Nd sintered magnets at 180 °C was narrower than that at 60 °C. The Pareto front range of the Nd sintered magnets was also narrower than that of the Nd sintered magnets at 60 °C. In particular, the higher grade of Nd sintered magnets could not reach the torque constraint due to thermal demagnetization, and the Pareto front could not be formed. The Pareto front range was also narrowed for the lower grade Nd sintered magnets, and the loss at P_2 was

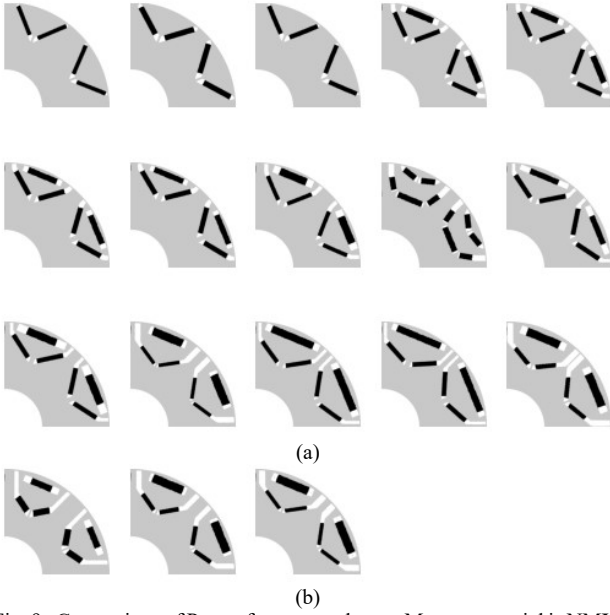


Fig. 9. Comparison of Pareto front rotor shapes. Magnet material is NMX-43EH, and magnet temperatures are (a) 60 °C and (b) 180 °C.

particularly large. In contrast, the Pareto front range of SmCo magnets, which have excellent high-temperature characteristics, remained almost the same at 60 °C and 180 °C, indicating that the motor characteristics can be maintained with low cooling power.

Fig. 9 shows a comparison of the Pareto front rotor shapes for NMX-43EH and different magnet temperatures. In higher-grade Nd sintered magnets, it is difficult to obtain torque at high temperatures due to thermal demagnetization. Therefore, while a variety of shapes exist on the Pareto front at low temperatures, only the Nabla shape, which is the easiest to obtain torque, exists at high temperatures due to the torque constraint.

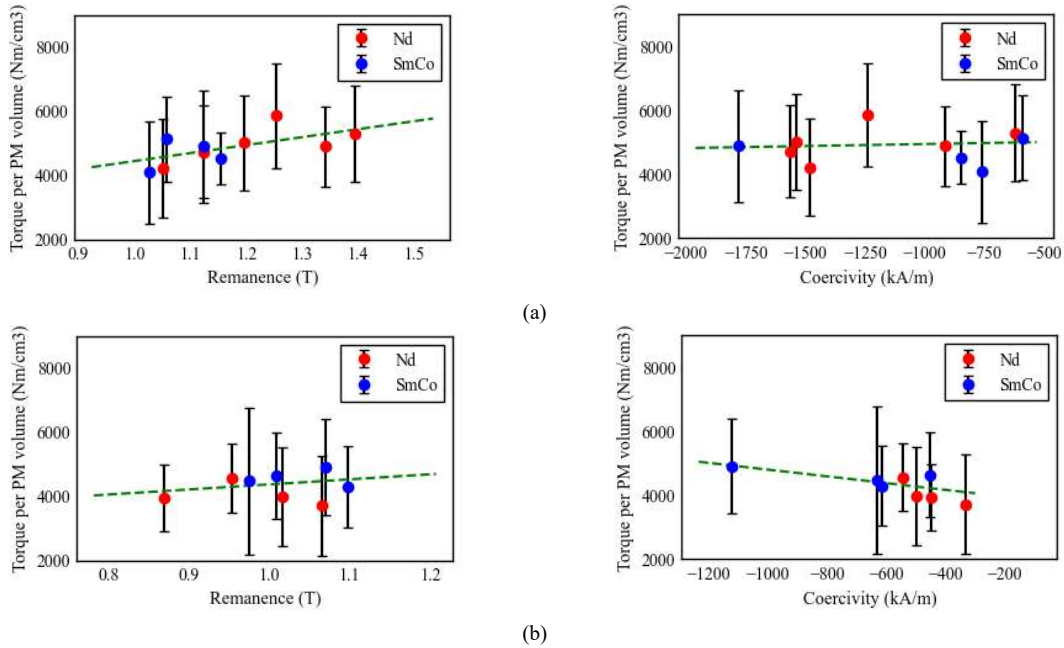


Fig. 10. Torque per PM volume of final population of torque maximization and PM volume minimization for different PM material for (a) 60 °C and (b) 180 °C. The round dots represent the mean values of the final population characteristics, and the error bars represent the maximum and minimum values. The green dashed line represents the linear regression.

B. PM Volume Minimization and Torque Maximization

Similarly, the multi-objective optimization of minimizing the PM volume and maximizing the torque is performed and differences in results due to PM material are discussed. The optimization problem is as follows.

$$\begin{aligned} \min_z \quad & (-T_{\max}^{\text{pred}}, V_{PM})^T, \\ \text{s.t.} \quad & g : T_{\max}^{\text{pred}} \geq \alpha T^{\text{req}}, \end{aligned} \quad (13)$$

where T_{\max}^{pred} is the predicted maximum torque, and V_{PM} is the PM volume. g is the required torque constraint for $T^{\text{req}} = 280$ Nm.

Fig. 10 shows the torque per PM volume for the last generation of individuals. However, the individuals that do not meet the maximum torque constraint of 280 Nm are not shown in the figure for optimization. First, at a PM temperature of 60 °C, the maximum torque showed an increasing trend due to the increase in magnet torque as the residual flux density increased. At 60 °C, the effect of thermal demagnetization was small and there was no correlation between the coercive force and the maximum torque per PM volume. Then, at a PM temperature of 180 °C, the torque per PM volume of the motor using Nd sintered magnets was significantly lower due to the effect of thermal demagnetization. In contrast, the results for SmCo magnets were almost the same as those at 60 °C, indicating that they are robust to temperature changes. Furthermore, as shown in the right side of Fig. 10(b), the negative correlation between coercive force and torque per PM volume is a spurious correlation due to the fact that motors using PMs with higher coercive force are less likely to be demagnetized.

IV. CONCLUSION

This paper proposed an automatic design system with variable PM material and PM temperature. By utilizing the short-term prediction capability of deep learning and performing geometry optimization under various conditions, it was found that motors using Nd sintered magnets have low

loss at low speeds and high torque per PM volume, but do not have excellent characteristics at high temperatures. On the other hand, the motor using SmCo magnets was found to have high loss at low speeds but high tolerance to temperature changes. Thus, the proposed system can perform a large amount of geometry optimization in a short time for various PM material conditions, and various quantitative insights are available from the results.

The limitation of the data-driven deep learning model proposed in this study is that its applicability is highly dependent on the dataset. To build a more general model, a richer motor design dataset is needed, and the most important issue is how to obtain such a dataset.

REFERENCES

- [1] Z. Pan and S. Fang, "Torque Performance Improvement of Permanent Magnet Arc Motor Based on Two-Step Strategy," *IEEE Trans. Ind. Inf.*, vol. 17, no. 11, pp. 7523–7534, Nov. 2021.
- [2] M.-S. Kwon and D.-K. Lim, "A Study on the Optimal Design of PMA-SynRM for Electric Vehicles Combining Random Forest and Genetic Algorithm," *IEEE Access*, vol. 11, pp. 52357–52369, 2023.
- [3] H. Sasaki, Y. Hidaka, and H. Igarashi, "Prediction of IPM Machine Torque Characteristics Using Deep Learning Based on Magnetic Field Distribution," *IEEE Access*, vol. 10, pp. 60814–60822, 2022.
- [4] Y. Shimizu, S. Morimoto, M. Sanada, and Y. Inoue, "Using Machine Learning to Reduce Design Time for Permanent Magnet Volume Minimization in IPMSMs for Automotive Applications," *IEEJ J. Ind. Appl.*, vol. 10, no. 5, pp. 554–563, 2021.
- [5] M. Oka and M. Enokizono, "Magnetic Property Evaluation of the High-Speed Motor Stator Core Under Sinusoidal and Pulse Width Modulation Wave Excitation Using the Stator Winding Excitation Method," *J. JSAEM*, vol. 27, no. 1, pp. 79–84, 2019.
- [6] Y. Shimizu, S. Morimoto, M. Sanada, and Y. Inoue, "Automatic Design System With Generative Adversarial Network and Convolutional Neural Network for Optimization Design of Interior Permanent Magnet Synchronous Motor," *IEEE Trans. Energy Convers.*, vol. 38, no. 1, pp. 724–734, Mar. 2023.
- [7] Y. Shimizu, "Efficiency Optimization Design That Considers Control of Interior Permanent Magnet Synchronous Motors Based on Machine Learning for Automotive Application," *IEEE Access*, vol. 11, pp. 41–49, 2023.
- [8] Liu *et al.*, "Swin Transformer: Hierarchical Vision Transformer using Shifted Windows," in *2021 IEEE/CVF International Conference on Computer Vision (ICCV)*, Oct. 2021, pp. 9992–10002.
- [9] Y. Shimizu, "Automatic Design System with Generative Adversarial Network and Vision Transformer for Efficiency Optimization of Interior Permanent Magnet Synchronous Motor," *IEEE Transactions of Indust.*
- [10] K. Deb, A. Pratap, S. Agarwal, and T. Meyarivan, "A fast and elitist multiobjective genetic algorithm: NSGA-II," *IEEE Trans. Evol. Comput.*, vol. 6, no. 2, pp. 182–197, Apr. 2002.
- [11] J. Blank and K. Deb, "Pymoo: Multi-Objective Optimization in Python," *IEEE Access*, vol. 8, pp. 89497–89509, 2020.

Yuki Shimizu received the B.E., M.E., and Ph.D. degrees from Osaka Prefecture University, Sakai, Japan, in 2016, 2018, and 2022, respectively. In 2018, he joined Toyota Motor Corporation, Aichi, Japan. In 2022, he joined the Graduate School of Science and Engineering, Ritsumeikan University, where he is currently an Assistant Professor. In 2023, he also

founded MotorAI, Inc., where he is currently the Chief Executive Officer. His main research interests are the design and control of permanent magnet synchronous motors using machine learning and deep learning.

Kan Akatsu received the B.S., M.S., and Ph.D. degrees in electrical engineering from Yokohama National University, Yokohama, Japan, in 1995, 1997, and 2000, respectively. He was with the Nissan Research Center, Yokosuka, Japan, in 2000. He contributed to the design and analysis of the new concept permanent magnet machines. In 2003, he was with the Department of Electrical and Electric Engineering, Tokyo University of Agriculture and Technology, Tokyo, Japan, as an Assistant Professor. From 2005 to 2007, he was a JSPS Postdoctoral Fellowship for Research Abroad, Visiting Professor with Wisconsin Electric Machines and Power Electronics Consortium, University of Wisconsin-Madison, Madison, WI, USA. From 2009, he was an Associate Professor, and he was a Full Professor with the Shibaura Institute of Technology, Tokyo, Japan. From October 2019, he is a Professor with Yokohama National University.